A Mathematical Analysis of Atomistic to Continuum Coupling Methods

Award DE-FG02- 05ER25697

Jacob Fish (PI) and Mark Shephard (co-PI)
Rensselaer Polytechnic Institute

Final Report

Summary
We development a general framework for information-passing and concurrent discrete to continuum scale bridging and applied it to biological, electro-mechanical and thermo-electrical systems. Funds were used for *partial* support of two post-doctoral research associates (Aiqin Li, Dawei Zhang) and three graduate students (Renge Li, Mohan Nuggehally, Joseph Riendeau).

1. Generalized Mathematical Homogenization (Fish, Chen, Li, 2007), (Li, Li, Fish, 2007)

1.1 The general framework

A prototype of the atomistic to continuum (AtC) coupling system is schematically illustrated in Fig. 1. The system consists of the following modules:

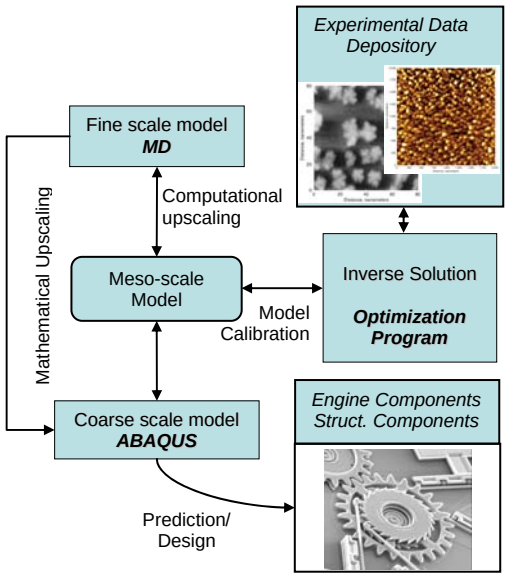

Fig. 1: AtC coupling system

a. *Mathematical upscaling*: derivation of coarse-scale equations directly from atomistic equations using Generalized Mathematical Homogenization theory (Fish, Chen, Li, 2007).

b. Computational upscaling: reducing the complexity of solving an atomistic problem to a manageable size that can be adapted based on available computational resources. Our model reduction approach is based on the space-time multilevel method (Li, Waisman, Fish, 2007). In the regions where the Generalized Mathematical Homogenization is estimated to be inaccurate (Nuggehally et al, 2007), a concurrent AtC bridging approach is employed (Fish et al, 2007) (Badia et al, 2007).

c. *Model calibration:* solving an inverse problem for calibration of fine scale parameters (interatomic potentials) by minimizing the error between the experimental data and multiscale simulations (Oskay, Fish, 2007).

1.2 Summary Governing Equations

The following thermo-mechanical continuum equations were derived directly from Molecular Dynamics (MD) equations with many body potential included (for derivation

details see (Fish, Chen, Li, 2007) for two body potentials, (Li, Li, Fish, 2007) for many body potentials)

1.2.1 *Atomistic unit cell problem*

$$m_i(\mathbf{Y}_i)\frac{\partial^2 \hat{\mathbf{u}}^1(\mathbf{X},\mathbf{Y}_i,t,t)}{\partial t^2} = e^2\Big[\sum_{j\neq i}\mathbf{f}_{ij}(\hat{\phi}_{ij}) + \sum_{(i,n_1,n_2,\ldots n_k)}\mathbf{S}_i(e\phi_{in_1}, e\phi_{in_2},\ldots e\phi_{in_k})\Big] \quad \forall i$$

where $\hat{\mathbf{u}}^1(\mathbf{X},\mathbf{Y}_i,t,t) = e\mathbf{u}^1(\mathbf{X},\mathbf{Y}_i,t,t)$. $(i,n_1,n_2,...,n_k)$ - many body interacting atoms $i,n_1,n_2,...,n_k$; $\mathbf{f}_{ij}$ and $\mathbf{S}_i$ are the forces acting on atom i from two-body and many-body potential term, respectively.

1.2. 2. *Macroscopic equations of motion*

$$\rho_0\frac{\partial^2 \mathbf{u}^0(\mathbf{X},t)}{\partial t^2} - \tilde{\nabla}_{\mathbf{X}}\cdot\langle\mathbf{P}\rangle = 0$$

$$\mathbf{P}(\mathbf{X},t,t) = \frac{1}{2\Omega}\Big\{\sum_{i=1}^{n}\sum_{j\neq i}[\mathbf{f}_{ij}(\hat{\phi}_{ij})\otimes\mathbf{X}_{ij}] + \sum_{i=1}^{n}\sum_{(i,n_1,n_2,\ldots n_k)}\Big[\sum_{j=n_1,n_2,\ldots n_k\neq i}(\mathbf{S}_{i(j)}\otimes\mathbf{X}_{ij})\Big]\Big\}$$

where $\mathbf{P}(\mathbf{X},t,t)$ is the First Piola-Kirchhoff stress tensor; $\mathbf{S}_{i(j)}$ is the many body force acting on atom i by atom j; Ω is the volume of a unit cell.

1.2.3. *Thermal equation*

$$C\frac{\partial\langle T\rangle}{\partial t} - \tilde{\nabla}_{\mathbf{X}}\cdot\langle\mathbf{q}(\mathbf{X},t,t)\rangle = 2\rho_0\frac{\partial\mathbf{u}^0(\mathbf{X},t)}{\partial t}\cdot\frac{\partial^2\mathbf{u}^0(\mathbf{X},t)}{\partial t^2}$$

$$\mathbf{q}(\mathbf{X},t,t) = \frac{1}{2\Omega}\sum_{i=1}^{n}\Big\{\frac{\partial\mathbf{u}_i^1}{\partial t}\cdot\Big[\sum_{j\neq i}(\mathbf{f}_{ij}\otimes\mathbf{X}_{ij}) + \sum_{(i,n_1,n_2,\ldots n_k)}\Big(\sum_{j=n_1,n_2,\ldots n_k\neq i}(\mathbf{S}_{i(j)}\otimes\mathbf{Y}_{ij})\Big)\Big]\Big\}$$

where $C = nk_BN_d/\Omega$ is heat capacity; $\mathbf{q}(\mathbf{X},t,t)$ the heat flux vector; n the number of atoms in unit cell; k_B the Boltzmann constant; N_d the number of degrees-of-freedom in each atom.

1.3 Algorithmic details and implementation

In the following we describe how to integrate a molecular dynamics code into a commercial finite element code of choice (we selected ABAQUS as a commercial FEM code). The coarse scale (continuum) and fine scale (atomistic) analyses were linked via ABAQUS user-defined subroutines UMAT() and UMATHT(). The overall algorithm is schematically depicted in Figure 2. At each integration point of the continua, load increment *n+1* and Newton iteration *i+1*, ABAQUS calls UMAT(mechanical fields) and UMATHT(thermal fields) routines to solve for the atomistic unit cell problem with coarse scale quantities, deformation gradient ($^{i+1}_{n+1}\mathbf{F}$), temperature ($^{i+1}_{n+1}\boldsymbol{\theta}$) and temperature gradient ($^{i+1}_{n+1}\boldsymbol{\theta}_{,\mathbf{X}}$) prescribed as external excitations. UMAT calculates the overall fields

including Cauchy stress ($^{i+1}_{n+1}\langle\boldsymbol{\sigma}\rangle$) and the homogenized instantaneous tangent modulus ($^{i+1}_{n+1}\langle\mathbf{L}\rangle$).

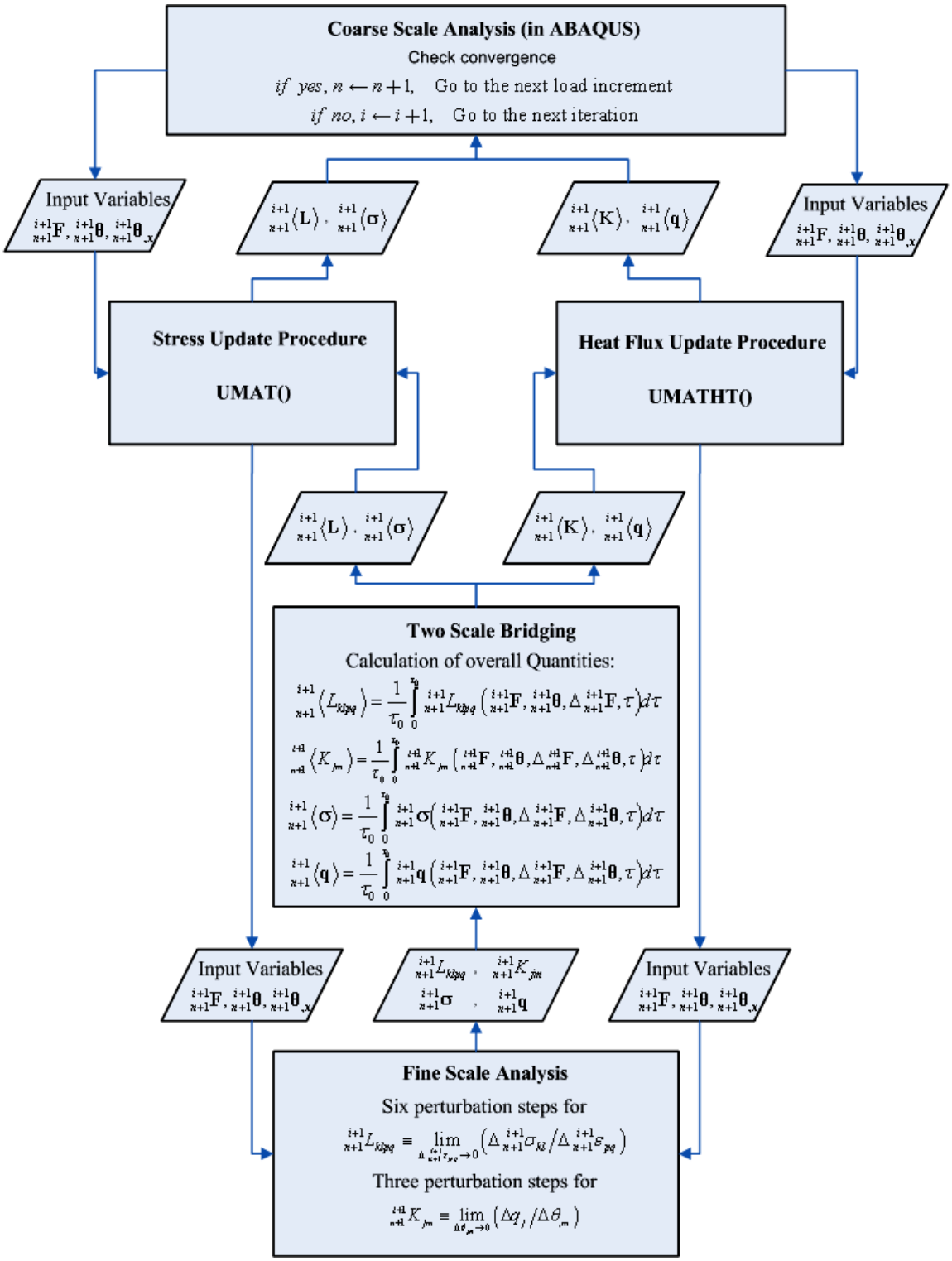

Figure 2: Program architecture for the two-scale AtC analysis using ABAQUS.

The UMATHT solves the atomistic unit cell problem for the fast temporal averaging quantity ${}^{i+1}_{n+1}\langle \mathbf{K} \rangle$ and the heat flux vector ${}^{i+1}_{n+1}\langle \mathbf{q} \rangle$. It then calculates the internal heat energy per unit mass increment ${}^{i+1}_{n+1}\Delta \mathbf{U}$ and updates internal heat energy ${}^{i+1}_{n+1}\mathbf{U} = {}_{n}\mathbf{U} + {}^{i+1}_{n+1}\Delta \mathbf{U}$. ${}^{i+1}_{n+1}(\bullet)$ denotes the $(i+1)^{\text{th}}$ iteration during the load increment $[t_n, t_{n+1}]$.

We employ a linear perturbation approach to calculate instantaneous properties. By this approach, a small coarse scale strain perturbation is applied onto the unit cell, and each column of ${}^{i+1}_{n+1}\mathbf{L}$ is extracted from $\Delta {}^{i+1}_{n+1}\boldsymbol{\sigma} = {}^{i+1}_{n+1}\mathbf{L} \cdot \Delta {}^{i+1}_{n+1}\boldsymbol{\varepsilon}$ where $\Delta {}^{i+1}_{n+1}\boldsymbol{\varepsilon} = \frac{1}{2}(\Delta {}^{i+1}_{n+1}\mathbf{F}^T \cdot \Delta {}^{i+1}_{n+1}\mathbf{F} - \mathbf{I})$. Six uniform Green-Lagrange strain increments $\Delta {}^{i+1}_{n+1}\boldsymbol{\varepsilon}$ are applied to evaluate six columns of ${}^{i+1}_{n+1}\mathbf{L}$. The resulting stress influence functions are determined by ${}^{i+1}_{n+1}L_{klpq} = \frac{1}{\Delta {}^{i+1}_{n+1}\varepsilon_{pq}} \Delta {}^{i+1}_{n+1}\sigma_{kl}$. The procedure for the calculation of instantaneous thermal properties ${}^{i+1}_{n+1}K_{jm}$ is similar except that there are three components of uniform temperature gradient in 3D.

1.4 Preliminary numerical results

Consider a model problem of a 3D beam (nano wire) depicted in Figure 3. The size of beam is $2000 \times 2000 \times 20000$. Note that all the units are normalized by $s = 2.0951 \text{Å}$. The beam is clamped at the left end with initial temperature of 20K. The surface flux, $q(t) = 10^{-5}$, is applied at the left end. In the first test problem, periodic pressure $p(t) = -0.005 \sin(6.28318 \times 10^{-5} pt)$ is applied at the right end. In the second test problem, $p(t) = -0.0001 \sin(6.28318 \times 10^{-5} pt)$ is applied on the top surface. The beam is discretized with the 8-node coupled temperature-displacement brick elements having four degrees of freedom per node (three displacement components and temperature). A unit cell consists of $2 \times 2 \times 2$ single silicon crystal cube having 95 atoms (Figure 3). The Stillinger-Weber potential is used.

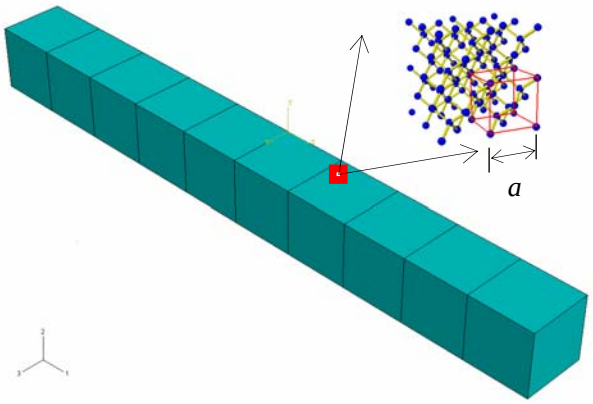

Figure 3: A 3D cantilever beam and unit cell models.

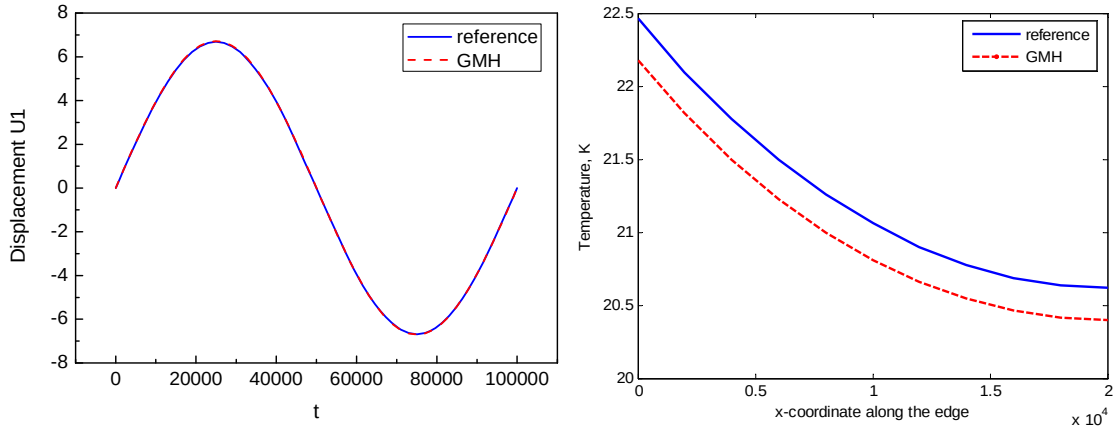

(a) Time history of nodal displacement (b) temperature distribution along the beam

Figure 4: Results of Example 1 with 10 elements. In this case pressure is applied on the right end.

The results of the first test problem are plotted in Figure 4. Figure 4(a) shows the time history of one nodal displacement at the right end. The temperature along one edge of the beam is shown in Figure 4(b).

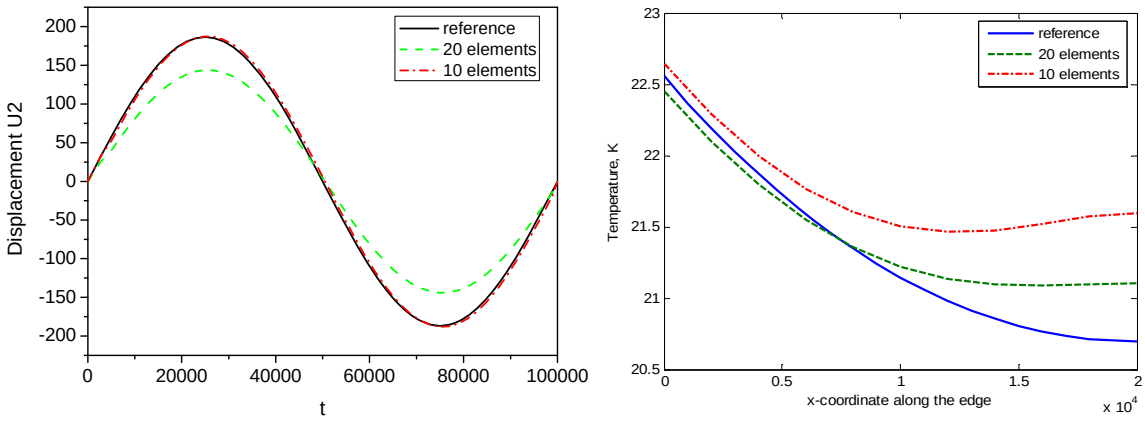

(a) Time history of nodal displacement (b) temperature distribution along the beam

Figure 5: Results of Example 2. In this case pressure is applied on the top surface.

The results of the second example are illustrated in Figure 5. Figure 5(a) shows the time history of one nodal displacement at the right end while the temperature along one edge of the beam is displayed in Figure 5(b).

The GMH agrees reasonably well with the results from traditional continuum mechanics. We are in the process of applying GMH to nanodevices were the classical continuum mechanics is expected to break down because of significant surface effects.

1.5. Generalized mathematical homogenization of ferroelectrics (Zhang, Riendeau, Fish, 2007)

The ferroelectric materials are widely used in actuators, capacitors, transducers, dynamic random access memory (DRAM) and non-volatile random access memory devices. Yet

to date, nearly all developments have centered on evaluating and "scaling" the high energy, short-range covalent bond forces into continuum descriptions with no rigorous theory that would feed atomistic data into continuum description. Our goal is to derive coupled electro-thermo-mechanical equations of continuum directly from the molecular dynamics equations of ferroelectric materials using Generalized Mathematical Homogenization theory. Some preliminary discussion is outlined below.

To account for electronic scale we adopt shell model originally proposed by Dick and Overhauser (1958). The shell model describes each polarizable ion or atom as a pair of point charges separated by a variable distance, as illustrated in Figure 6. A "core" charge $z_i + q_i$ is attached by a harmonic (or anharmonic) spring with spring constant k_i (or k_{2i} and k_{4i}) to a "shell" charge $-q_i$. The center of mass is at or near the core charge. The magnitudes of both the core and shell charges are fixed in the shell model. The polarization thus occurs via relative displacement of the core and shell charges. As with any model involving inducible dipoles, the potential energy of the induced dipoles contains terms representing the interaction with any static field, the interaction with other dipoles, and the polarization energy. Both displacements of the core, shell and electric fields are expanded in space-time asymptotic expansions and macroscopic equations are derived (Zhang, Riendeau, Fish, 2007)

$$\rho_0 \frac{\partial^2 \mathbf{u}^0(\mathbf{X},t)}{\partial t^2} - \nabla_{\mathbf{X}} \cdot \langle \mathbf{P}_S(\mathbf{X},t,\tau) \rangle = \frac{\varepsilon}{\Theta} \left\langle \sum_{i=1}^{N} \sum_{j \neq i}^{N} \mathbf{f}'_{ij}(\varepsilon \phi_{ij}) \cdot (\mathbf{d}_j - \mathbf{d}_i) \right\rangle,$$

where d_i is the relative displacement of an electron cloud from the core.

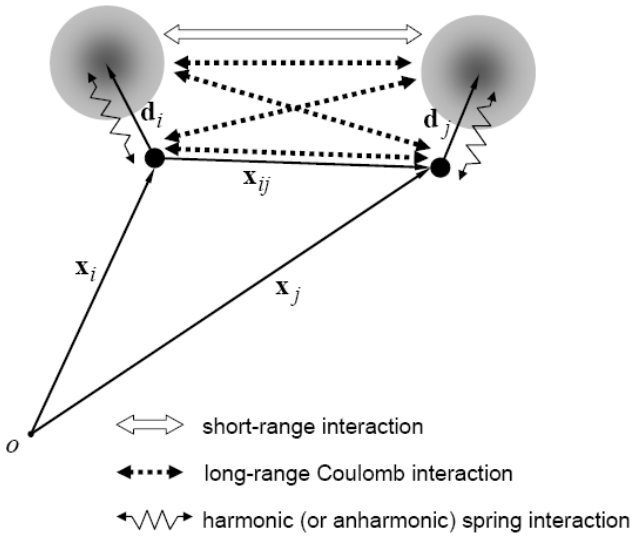

Fig. 6: Shell model

2. Space-Time Reduced Order Multilevel Method

To reduce the computational complexity of fine scale computations, we developed a space-time reduced order method (STRO) method (Li et al, 2007) for molecular dynamics simulations of biomolecules. The goal of the STRO is to reduce the computational cost of molecular dynamics simulations without loss of accuracy in the

quantities of interest. The method consists of the waveform relaxation scheme aimed at capturing the high frequency motions and a coarse scale solution in space and time aimed at resolving smooth features (in both space and time domains) of the system.
The coarse model correction $\mathbf{u}^{\mathrm{f}} + \mathbf{Q}\mathbf{e}^{\mathrm{C}}$ is calculated from the Hamilton principle on the subspace of coarse scale functions,

$$H(\boldsymbol{e}^c) = \sum w^f \left(\boldsymbol{u}^f + Q\boldsymbol{e}^c\right) + \sum \frac{1}{2} m \left(\dot{\boldsymbol{u}}^f + Q\dot{\boldsymbol{e}}^c\right)^T \left(\dot{\boldsymbol{u}}^f + Q\dot{\boldsymbol{e}}^c\right) \rightarrow \min_{e^c}$$

where $\mathbf{Q}$ is the interscale transfer operator; it depends on the choice of the coarse scale model. We have used the proper orthogonal decomposition (POD) modes for constructing the interscale transfer operator $\mathbf{Q}$. The accuracy and efficiency of this method was reported by applying it to a model problem of chain of α-D-glucopyranose monomers as shown in Fig. 7.

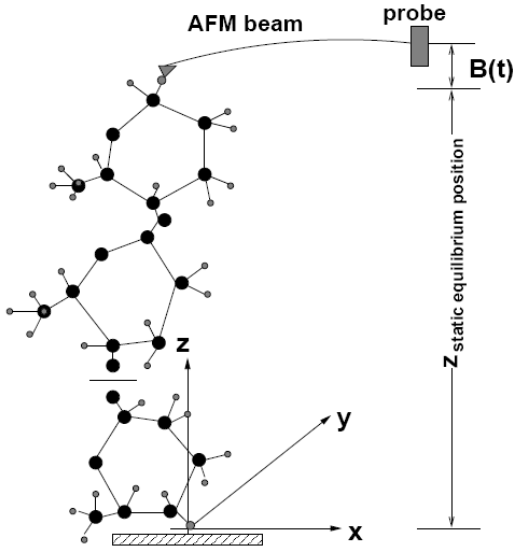

Fig. 7: Schematic diagram for stretching of the molecule by an AFM

Fig. 8 illustrates the relative CPU time on a single processor machine by POD based space-time multilevel method compared to the time cost of time marching the original system by Explicit Newmark method. As the number of modes included decreases the allowable integration time step increases. With POD based space-time multilevel method, the simulation can be orders of magnitude faster than the original explicit time marching method. These time savings have been obtained without compromising on solution accuracy in the quantities of interest.

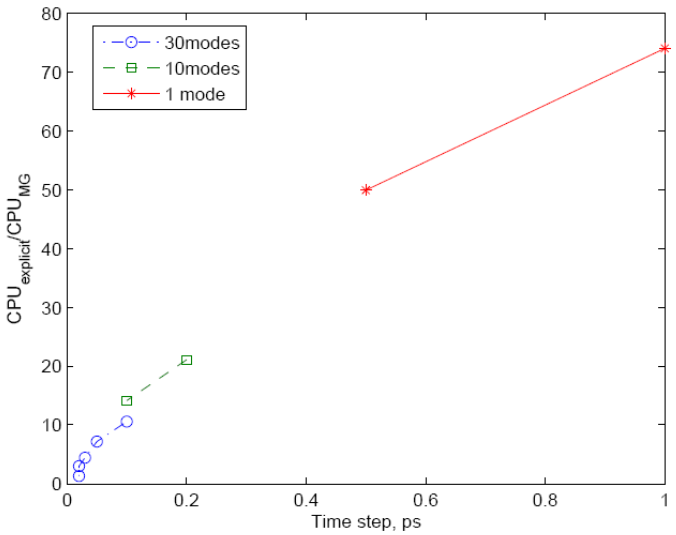

Fig. 8: Relative time vs. time step for different numbers of modes included in POD based space-time multilevel method.

3. Concurrent domain decomposition based multiscale model

A concurrent domain decomposition coupling method based on blending of continuum stresses with atomistic forces was developed (Fish et al, 2007, Badia et al, 2007). The problem domain is decomposed into an atomistic sub-domain where fine scale features need to be resolved, a continuum sub-domain which can adequately describe the macroscale deformation and an overlap interphase sub-domain that has a blended description of the two. The problem is formulated in terms of equilibrium equations with a blending between the continuum stress and the atomistic force in the interphase. Coupling between the continuum and the atomistics is established by imposing constraints between the continuum solution and the atomistic solution over the interphase sub-domain in a weak sense. Specifically, in the examples considered here, the atomistic domain is modeled by the Aluminum Embedded Atom Method (EAM) inter-atomic potential and the continuum domain is a linear elastic model consistent with the EAM potential.

The formulation was subjected to patch tests to demonstrate its ability to represent the constant strain modes and the rigid body modes. Figure 9 shows the hybrid atomistic-continuum domain considered for the patch tests. The constant strain modes and the rigid body modes are imposed through the appropriate Dirichlet boundary conditions to the continuum. The example consists of 13,075 total degrees of freedom out of which 12,147 were atomistic degrees of freedom and 928 were continuum degrees of freedom. Figure 10 shows that the displacements solved by the AtC concurrent method is consistent with the imposed strain modes for the case of a normal strain mode and a shear strain mode. These strains are well within the linear elastic regime of stress-strain response of the Aluminum lattice.

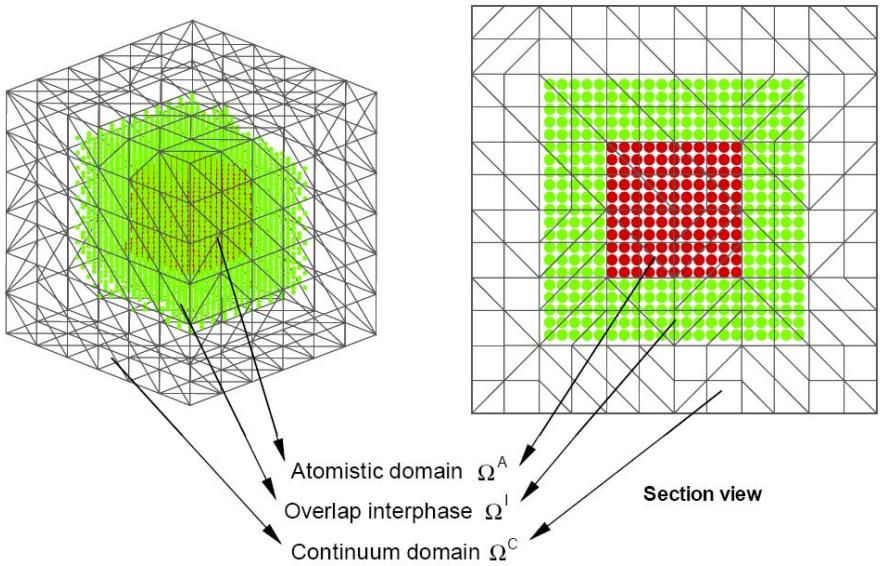

Figure 9: Hybrid atomistic-continuum domain for patch tests

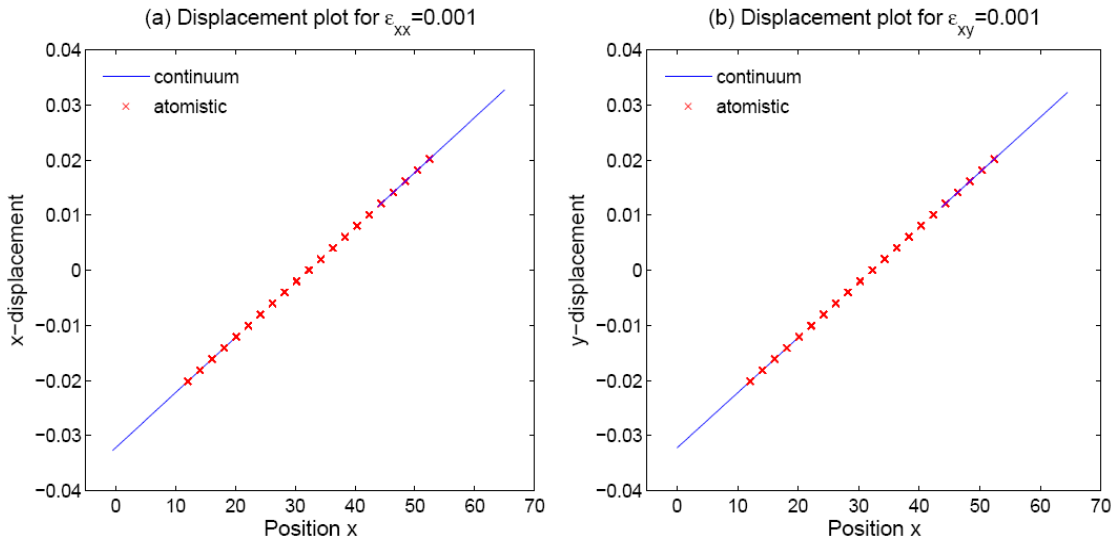

Figure 10: Displacement along X direction

We have also studied the method on two numerical examples: nano-indentation of a thin film and nano-void subjected to hydrostatic loading. Numerical results were reported in (Fish et al, 2007), (Nuggehally et al, 2007), (Badia et al, 2007). Methods for adaptive selection of an appropriate scale based on local error indicators were reported in (Nuggehally et al, 2007).

3.1 Adaptive Multiscale Concurrent Framework

To be able to select models from the hierarchy to minimize the modeling error, two error indicators are needed. The indicators employed in this work focus on defining and capturing the boundaries of domains within which various models in the hierarchy are required (i.e. the region within which a non-linear model is required, and the region within which the atomistic model is required). The sequence of steps in the adaptive procedure are as follows:

1. Start the load step of a quasi-statically loaded problem with a coarse model. (Note: Scale the load to a value where more than a linear elastic model is needed to solve the problem.)
2. Increment the load step.
3. Solve the problem with the concurrent model problem formulation.
4. Compute error indicators for the model hierarchy chosen.
5. Select or de-select the models from the hierarchy for sub-domains of the problem domain according to the error indicators and corresponding tolerance values.
6. If models change, go to step 3, else continue with step 2 until the final load is reached.

3.2 Verification of adaptive multiscale concurrent method

For the examples that follow, the constitutive parameters of the continuum nonlinear and linear elastic models are consistent with the EAM potential of Aluminum. The cubic elastic constants for aluminum are C_{11}=0.1181MPa, C_{12}=0,0623MPa, C_{44}=0.0367MPa.

3.2.1 Nano-indentation

A comparison of the three-model hierarchy with that of a two-model hierarchy (consisting of only the atomistic model and the linear elastic model) is given here. The problem domain is a film of approximately 30 nm thickness placed on a rigid substrate. The indenter is rectangular in shape and approximately 1.87 nm wide. The indenter and film are considered to be infinite in the *x* direction (out of plane); thus a plane strain condition exists. Homogeneous Dirichlet boundary conditions are imposed in *z* on the bottom face, and in *y* on the left and right faces. The indenter load is applied quasi-statically through a Dirichlet boundary condition by moving it by 0.005 nm for each load step. Periodic boundary conditions in are imposed on the atomistic model to maintain a 3D lattice structure. The crystallographic orientation chosen is such that the dislocations generated from the corners of the indenter move straight into the material. Fig. 11 shows the results of the simulation at load step 60. The three-model hierarchy created about 6500 atoms, while the two-model hierarchy produced about 13600 atoms. The total energy computed from the two models was roughly the same (see Fig. 12), indicating that the same accuracy for the solution was computed with about a third of the computational cost. For the solution accuracy obtained for the a priori mesh used in examples, the atomistic indicator tolerance predicts dislocation nucleation correctly with respect to a fully atomistic model

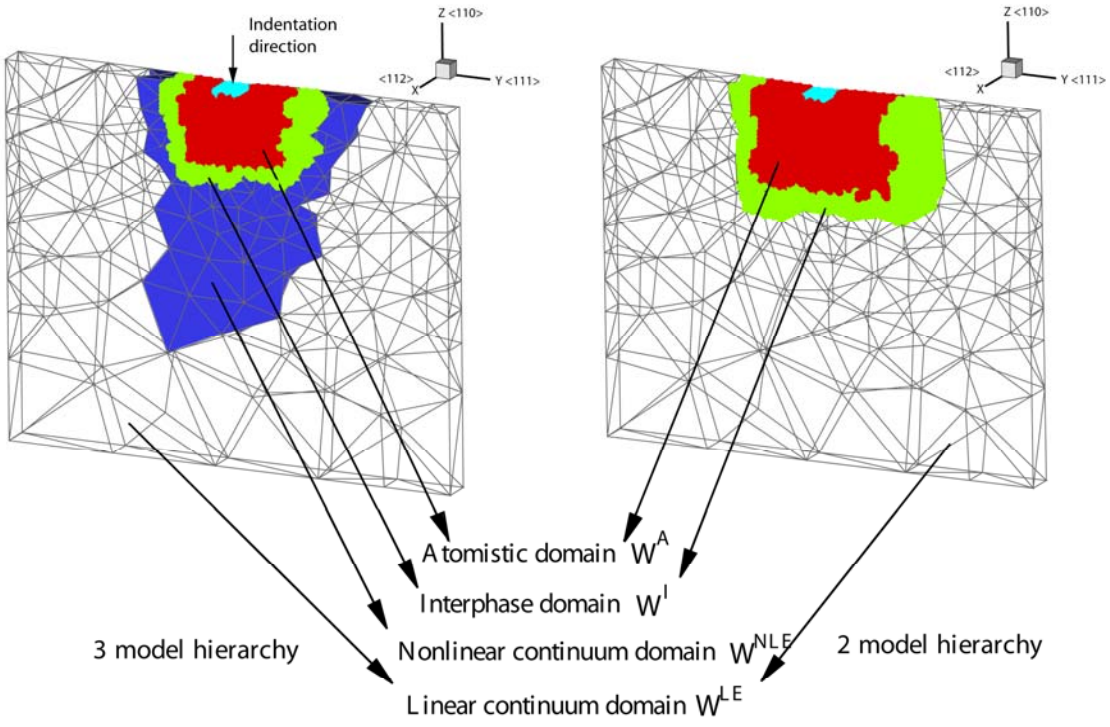

Figure 11: Two hierarchical concurrent models at load step 60.

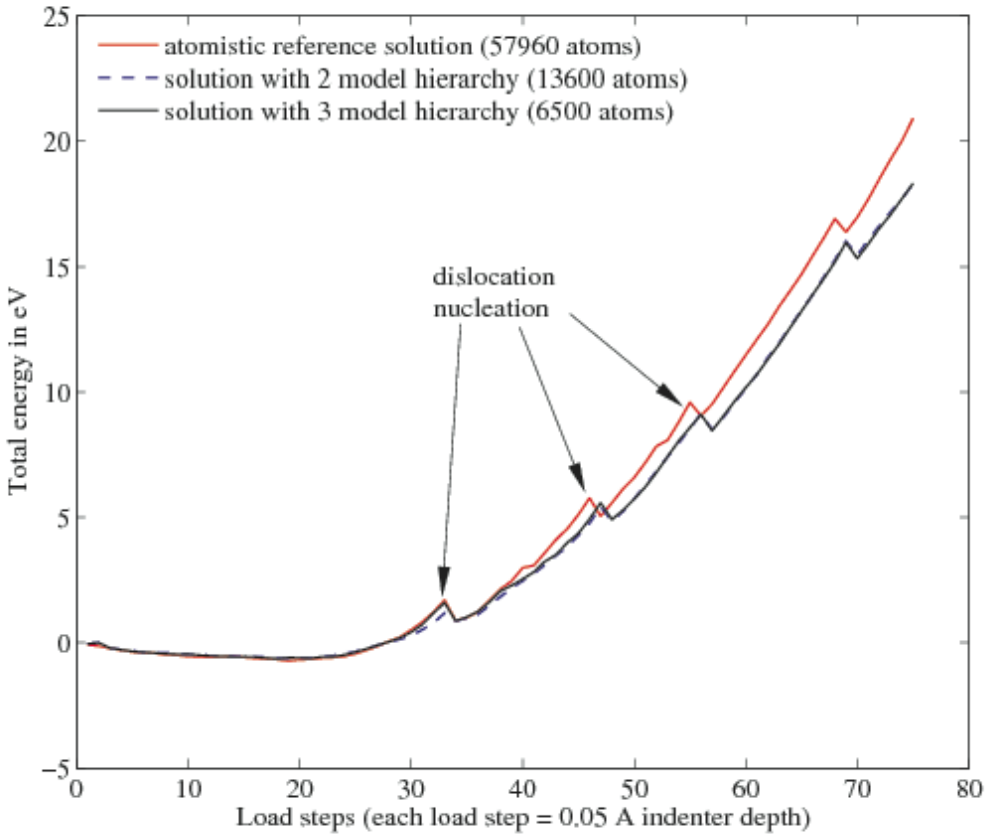

Figure 12. Energy comparison between atomistic reference solution and concurrent models with different hierarchy

3.2.2. Nano-void subjected to hydrostatic load

Adaptive model refinement and model coarsening is demonstrated here for the case of a nano-void subjected to a cycle of hydrostatic loading/unloading. The problem domain is a cube of approximately 50nm edge length with a spherical void of approximately 5nm diameter at the center. The load is applied quasi-statically in small increments of 0.0375nm on each face of the cube through Dirichlet boundary conditions. The simulation of a nano-void subjected to hydrostatic load has been used to study nano-void growth and cavitation.

The load is applied during the first 23 load steps, followed by subsequent unloading for the following 23 load steps. At each load step the problem is solved using the concurrent model of the previous load step. Models in the hierarchy are adaptively changed based on the error indicators computed for the current load step.

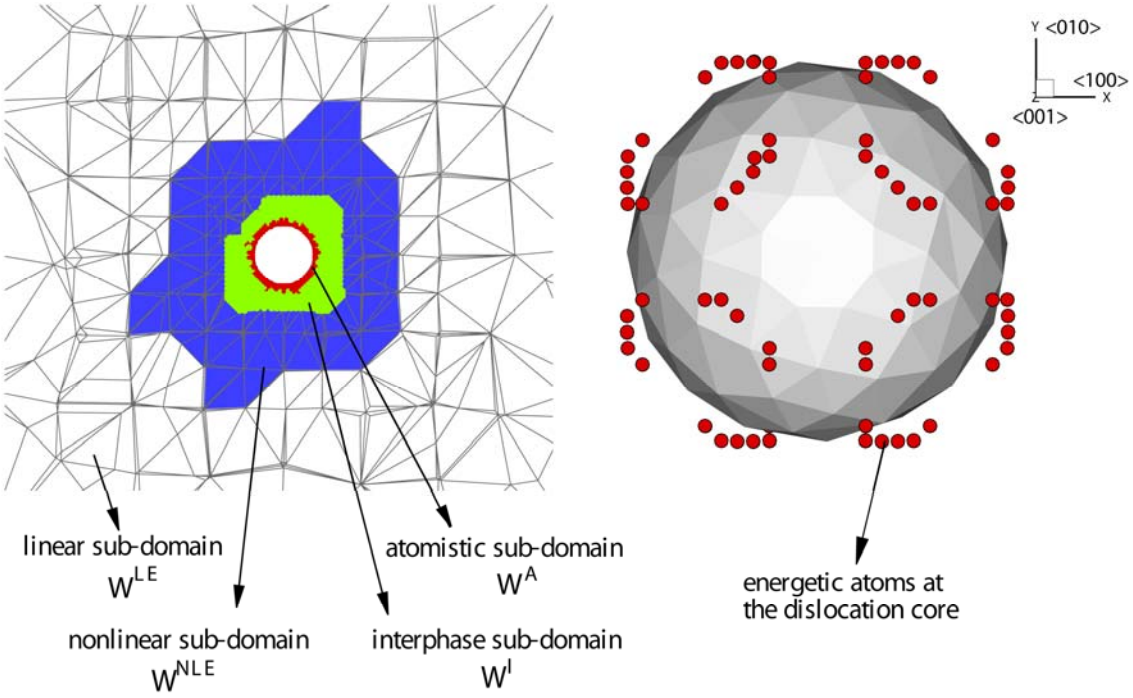

Figure 13: The concurrent model and dislocation loops observed at load step 18.

Fig. 13 shows the concurrent model at load step 18 and the dislocation loops that are observed to just nucleate from the void surface at this load step. The atomistic model consists of 20190 atoms. These dislocation loops grow and react to form Lomer-Cottrell junctions as seen in the right side of Fig. 14. These junctions result in stacking fault tetrahedra around the void. The most energetic atoms located along the edges of these tetrahedra (dislocation cores) are shown in the right side of Fig. 14, while the left side shows the concurrent model at the corresponding load step. The atomistic model at load step 23 consists of 69070 atoms. The results obtained matched well with a fully atomistic solution to the problem. The model is unloaded gradually back to the initial stage. The reaction products of the dislocation structures formed during the unloading stage remain and can be seen in the right side of Fig. 15. Also note that the atomistic model has shrunk in size compared to that at maximum load. The left portion of Fig. 15 shows the concurrent model at the end of the simulation, which consists of 55763 atoms. However, the atomistic model is still used due to the presence of dislocation reaction debris.

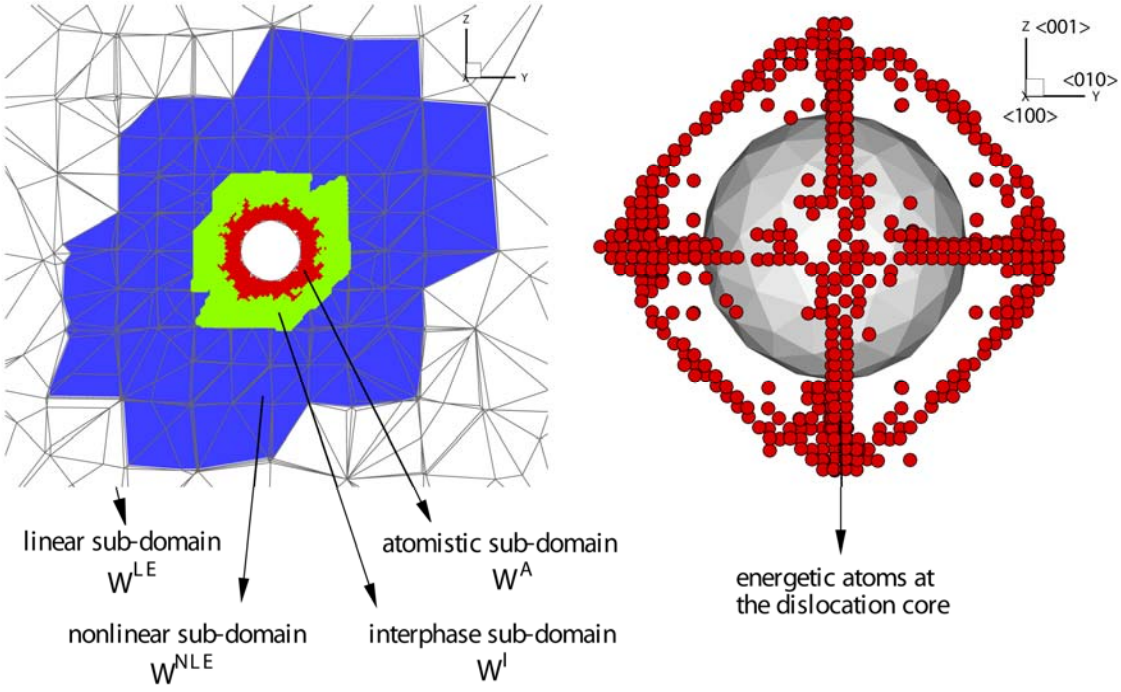

Figure 14: The concurrent model and stacking fault tetrahedra around the void at load step 23.

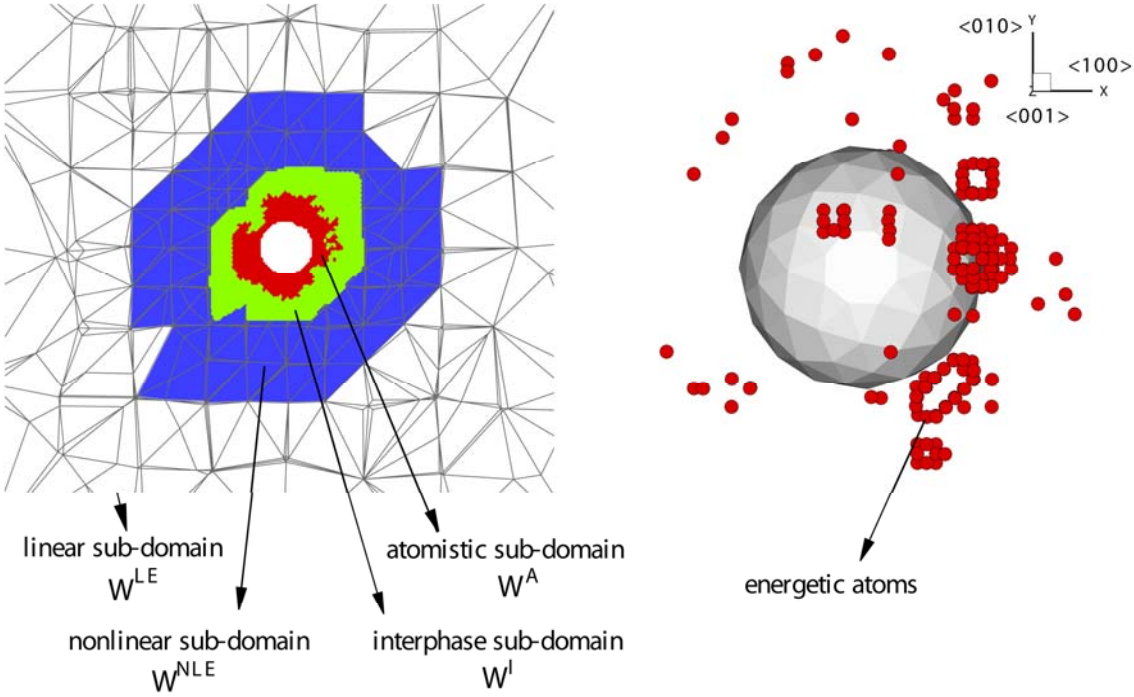

Figure 15: The concurrent model and reaction products of stacking fault tetrahedra at load step 46.

3.2.3 Nano-porous block subjected to compression:

The problem domain of a nano-porous block of material is idealized by a rectangular block of size 25nm X 25nm X 50nm with spherical nano-voids randomly distributed in it. An interesting physical phenomenon is the effect of the size of nano-voids, at a given porosity, on the stress-strain behavior of the material under compression is studied. Porosity can be quantified in terms of volume fraction defined as the ratio of total volume of the voids to the volume of the block of material. Materials with different size nano-voids are considered holding the volume fraction constant. At a given size of the nano-void different samples of the material block with random position of nano-voids are considered for the study.

A finite element discretization of the problem domain for a chosen volume fraction of 0.0164 and the nano-void size of 3.6 nm in diameter is shown in the left side of Figure 16. There are 21 randomly positioned nano-voids in the problem domain. The block is subjected to compression. Load is applied quasi-statically in −Z direction on top face and +Z direction on the bottom face by means of Dirichlet boundary condition. Side faces are traction free. In order to avoid the effect of hard walls at the top and bottom surfaces anti-periodicity in Z is imposed to mimic the behavior of a long nano-porous column.

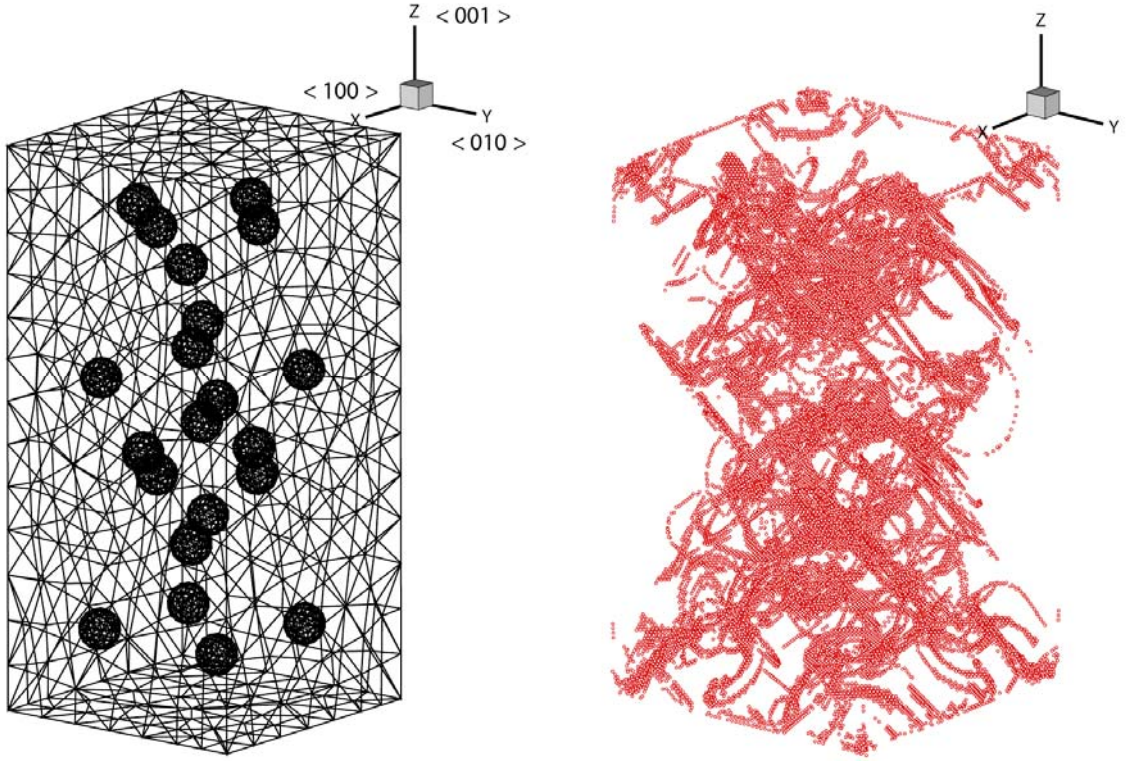

Figure 16: Finite element discretization of the problem domain and dislocation structures at a strain $\varepsilon_{33} = 0.10$

The problem domain is discretized with tetrahedral elements such that the mesh is finer at the void surface and is gradually coarser away. This is because of the fact that void

surfaces are the critical regions that act as sites of dislocation nucleation. The mesh shown in the left side of Figure 16 consists of 95,647 regions. By the load step of total strain of 6.4% the problem domain is transformed completely into atomistic model with 1,932,692 atoms. Right half of Figure 9 shows the dislocation structures at the load step of total strain of 10%. At the beginning of the simulation, a load step with the linear elastic continuum model took 328 sec. Towards the end of the simulation the problem domain was fully atomistic. Atomistic model calculations were performed on 32 processors and it took 460 sec for a load step with a fully atomistic model. Calculations were performed on AMD Opteron 2.2 GHz processors.

Figure 17 shows the comparison of the stress-strain curves for different size mesh elements for the problem domain with 21 voids. This comparison was done to make sure results are not affected by the mesh size. Two meshes with 189,224 elements and 95,647 elements yield nearly same stress-strain curves while a coarser mesh with 23,278 elements yields stress-strain curve differs. This indicates a less accurate solution at the continuum level, which results in less accurate atomistic indicator and the atomistic sub-domain.

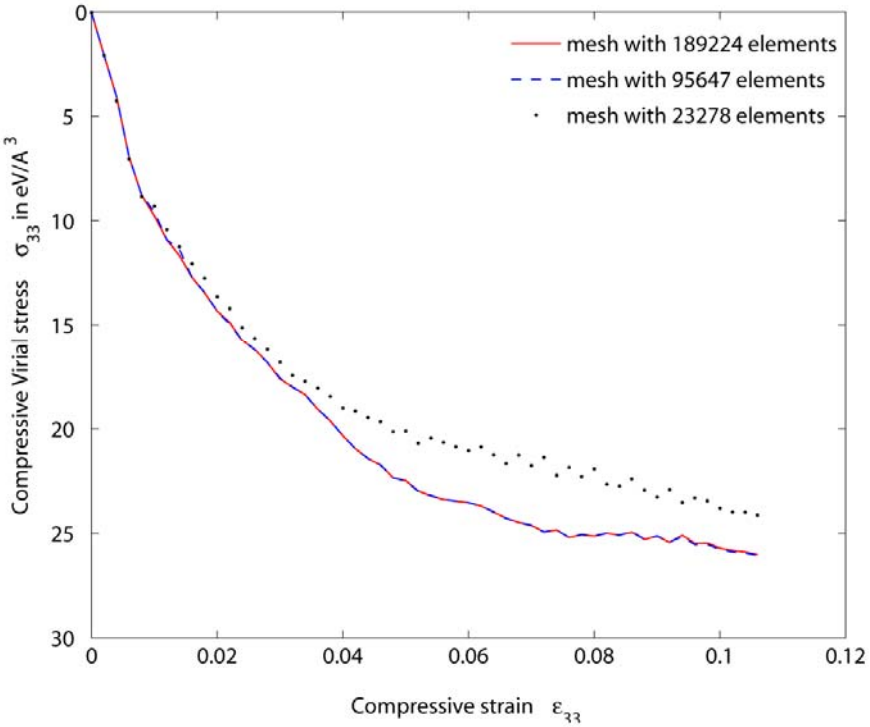

Figure 17: Comparison of the normal Virial stress σ_{33} v/s the normal strain ε_{33} for different mesh sizes for 3.6nm 21 void case.

Figure 18 shows the compressive Virial stress σ_{33} against the normal strain ε_{33} for three different void sizes at a volume fraction of 0.0164 For a given volume fraction and smaller the size of the voids, the greater the number of voids present in the block of material and smaller the distance between the voids. At the selected volume fraction, for

the void size of 3.6 nm there are 21 voids in the block of material, for the void size of 4.61 nm there are 10 voids and for the void size of 9.94 nm there is one void. Figure 18 shows that the material is stronger with the smaller size voids. This behavior can be attributed to the hardening associated with dislocation interaction. For the smaller void case, the dislocation nucleation and dislocation interaction is more intense since there are more voids which act as sources of dislocation nucleation, which interact at a closer range making the material harder.

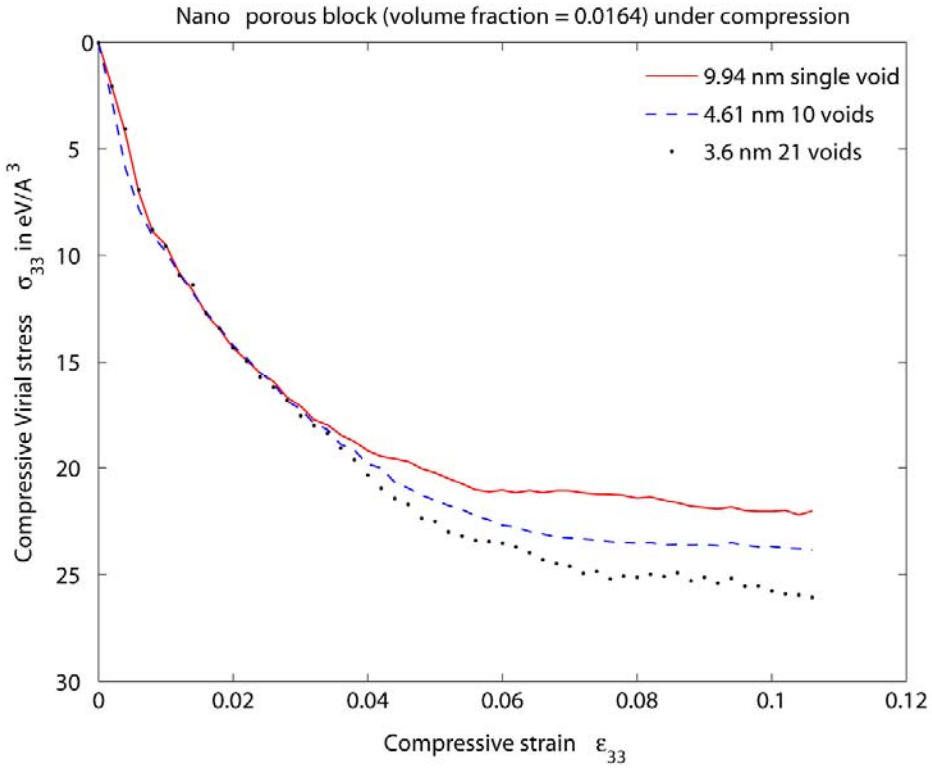

Figure 18: Variation of normal virial stress σ_{33} with the normal strain ε_{33} for different nano-void sizes. Stress computed at the top surface

The Influence of using parallel computation for the atomistic calculation while the continuum calculations are done in serial is studied for the simulation of the example with 10 voids of size 4.61 nm. Time taken for the atomistic calculations is 102,372 seconds. The time taken for the serial part of calculations is 7583 seconds. Parallel speedup is defined as

$$s(p) = \frac{t(s)}{t(p)}$$

where $t(s)$ is time for single processor and $t(p)$ is the time for p processors

Since ~ 93 % of the time is spent on atomistic calculation acceptable parallel speedups are obtained on systems up to several dozen processors (Fig. 19).

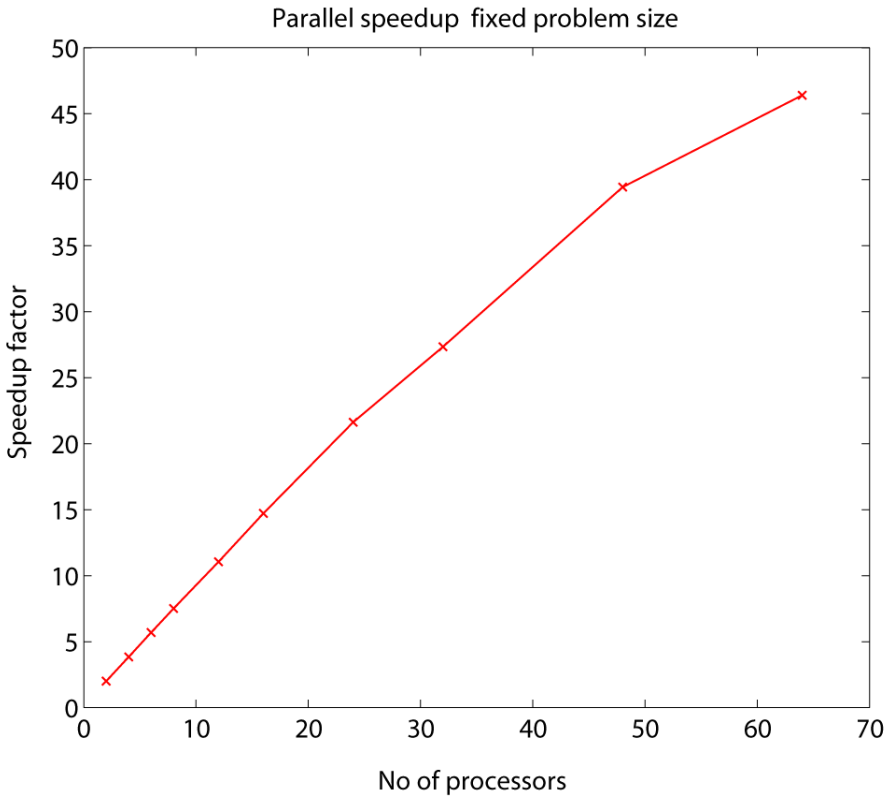

Figure 19: Parallel speedup for the atomistic calculations

This example is a first step towards understanding the phenomena of variation in yield stress related to volume fraction of the voids and the size of the voids in the nano-porous materials.

References

[1] J. Fish, W. Chen, R. Li, "Generalized mathematical homogenization of atomistic media at finite temperatures in three dimensions," Comp. Meth. Appl. Mech. Engng., Vol. 196, pp. 908-922, (2007)
[2] A. Li, R. Li and J. Fish, "Generalized Mathematical Homogenization: From Theory to Practice," Comp. Meth. Appl. Mech. Engng. (2009) 10.1016/j.cma.2008.12.038.
[3] A. Li, H. Waisman, and J. Fish, "A space-time multiscale method for molecular dynamics simulation of biomolecules," International Journal of Multiscale Computational Engineering, Vol. 4, No 5-6, pp. 791-803, (2006).
[4] M. A. Nuggehally, M. S. Shephard, C. R. Picu and J. Fish, "Adaptive Model Selection Procedure for Concurrent Multiscale Problems," Int. J. for Multiscale Computational Engineering Vol. 5, Issue 5, pp.369-386 (2007.)
[5] B. G. Dick, and A. W. Overhauser, "Theory of the Dielectric Constants of Alkali Halide Crystals," Physical Review 112 (1958), 90-103.

[6] J. Fish, M. A. Nuggehally, M. S. Shephard, C. R. Picu, S. Badia, M. L. Parks and M. Gunzburger “Concurrent AtC coupling based on a blend of the continuum stress and the atomistic force,” Comp. Meth. Appl. Mech. Engng., Vol. 196, Issue 45, pp. 4548-4560, (2007)
[7] S. Badia, P. Bochev, J. Fish, M. Gunzburger, R. Lehoucq, M. Nuggehally, M. L. Parks, "A Force-Based Blending Model for Atomistic-to-Continuum Coupling," Int. J. for Multiscale Computational Engineering, Volume 5, Issue 5, pp. 369-386, 2007.
[8] C. Oskay and J. Fish, “On Calibration and Validation of Eigendeformation-Based Multiscale Models for Failure Analysis of Heterogeneous Systems”, Computational Mechanics, Volume 42, Number 2, pp. 181-195, (2008).
[9] J. Fish, W. Chen, R. Li, “Generalized mathematical homogenization of atomistic media at finite temperatures in three dimensions,” Comp. Meth. Appl. Mech. Engng., Vol. 196, pp. 908-922, (2007)
[10] B. G. Dick, Jr. and A. W. Overhauser. Theory of the Dielectric Constants of Alkali Halide Crystals. Phys. Rev. 112, 90 - 103 (1958)